energies

MDPI

Article

Thermal, Microstructural and Electrochemical Hydriding Performance of a $Mg_{65}Ni_{20}Cu_5Y_{10}$ Metallic Glass Catalyzed by CNT and Processed by High-Pressure Torsion

Ádám Révész [1,*], Marcell Gajdics [2], Miratul Alifah [1], Viktória Kovács Kis [2,3], Erhard Schafler [4], Lajos Károly Varga [5], Stanislava Todorova [6], Tony Spassov [6] and Marcello Baricco [7]

[1] Department of Materials Physics, Eötvös University, P.O. Box 32, H-1518 Budapest, Hungary
[2] Center of Energy Research, Hungarian Academy of Sciences, H-1121 Budapest, Hungary
[3] Department of Mineralogy, Eötvös University, Pázmány Péter Sétány 1/c, H-1119 Budapest, Hungary
[4] Physics of Nanostructured Materials, Faculty of Physics, University of Vienna, A-1090 Vienna, Austria
[5] Research Institute for Solid State Physics and Optics, Hungarian Academy of Sciences, P.O. Box 49, H-1525 Budapest, Hungary
[6] Department of Chemistry, University of Sofia "St. Kl. Ohridski", 1164 Sofia, Bulgaria
[7] Dipartimento di Chimica and NIS-INSTM, Università di Torino, Via P. Giuria 7, 10125 Torino, Italy
* Correspondence: revesz.adam@ttk.elte.hu

Abstract: A $Mg_{65}Ni_{20}Cu_5Y_{10}$ metallic glass was produced by melt spinning and was mixed with a 5 wt.% multiwall carbon nanotube additive in a high-energy ball mill. Subsequently, the composite mixture was exposed to high-pressure torsion deformation with different torsion numbers. Complimentary XRD and DSC experiments confirmed the exceptional structural and thermal stability of the amorphous phase against severe plastic deformation. Combined high-resolution transmission electron microscopy observations and fast Fourier transform analysis revealed deformation-induced Mg_2Ni nanocrystals, together with the structural and morphological stability of the nanotubes. The electrochemical hydrogen discharge capacity of the severely deformed pure metallic glass was substantially lower than that of samples with the nanotube additive for several cycles. It was also established that the most deformed sample containing nanotubes exhibited a drastic breakdown in the electrochemical capacity after eight cycles.

Keywords: metallic glass; melt spinning; high-pressure torsion; hydrogen storage

Citation: Révész, Á.; Gajdics, M.; Alifah, M.; Kovács Kis, V.; Schafler, E.; Varga, L.K.; Todorova, S.; Spassov, T.; Baricco, M. Thermal, Microstructural and Electrochemical Hydriding Performance of a $Mg_{65}Ni_{20}Cu_5Y_{10}$ Metallic Glass Catalyzed by CNT and Processed by High-Pressure Torsion. *Energies* **2022**, *15*, 5710. https://doi.org/10.3390/en15155710

Academic Editor: Claudia Barolo

Received: 12 July 2022
Accepted: 4 August 2022
Published: 5 August 2022

1. Introduction

Alternative energy sources are barely competitive with conventional fossil fuels at the moment; nevertheless, hydrogen as a secondary energy carrier has received rapidly growing attention in the last several decades, mainly due to its very high chemical energy (120–140 MJ/kg) [1]. Hydrogen is clean, renewable and environmentally friendly; however, significant economic and technical challenges should be solved, including efficient production and storage [2]. Recently, a large number of attempts have been made to realize hydrogen storage in the solid state with sufficient storage capacity [3,4].

Among different hydrogen absorbing systems, magnesium-based alloys and compounds have been intensively investigated because of their high H-storage capacities (3700 Wh/L or 2600 Wh/kg), high abundance on Earth, low density, non-toxic nature and low cost, resulting in a potential candidate for future industrial applications [5–9]. Unfortunately, the relatively high hydrogenation enthalpy of Mg and its sluggish sorption kinetics are the main difficulties that still impede the widespread practical utilization of the Mg-H system [5,6]. In order to overcome these limitations of magnesium, different non-equilibrium techniques, such as rapid quenching by melt spinning and copper mold cast-

ing and high-energy ball milling (HEBM), have been applied to synthesize Mg-based hydrogen storage materials, including Mg-TM-RE ternary or pseudoternary systems (TM: transition metal; RE: rare earth element) [10]. The as-quenched alloy can contain fully crystalline phases [11,12], supersaturated solid solution [13], partial amorphous structure [14], or monolithic amorphous glassy phases [15,16].

It was reported that fully amorphous melt-spun $Mg_{60}RE_xNi_{30-x}Cu_{10}$ alloys can absorb 3.0 wt.% H_2 at a temperature as low as 130 °C. The enhanced hydrogenation rate was explained by the formation of hydrogen-induced phase separation [17]. A similar Mg-Ni-Ce system exhibits a hydrogen-induced glass-to-glass transition with a storage capacity of 5 wt.% H_2, which is considerably higher than the value obtained for the crystalline counterpart due to the disordered atomic structure and free volume of the glass [18]. A similar phenomenon was reported for the amorphous $Mg_{87}Ni_{12}Y_1$ alloy, which also exhibits faster H-sorption kinetics than partially or fully crystallized alloys due to the faster diffusion of the H atoms in the amorphous matrix; however, the storage capacity is practically independent of the atomic structure [19]. Excellent hydrogenation/dehydrogenation cycling performance was reported for the rapidly quenched partially crystalline $Mg_{80}Ni_{10}Y_{10}$ alloy [20], while the $Mg_{12}YNi$ solid solution exhibited enhanced H-kinetics due to the catalytic effects of Mg_2Ni and Y [13]. Due to the low mixing enthalpy between Ni and Y (ΔH = −25 kJ/mol), the activation energy of crystallization of melt-spun $Mg_{85}Ni_5Y_{10}$ can exceed 291 kJ/mol, indicating that atomic rearrangement is difficult due to interaction between these two elements [21]. In situ XRD analysis carried out during continuous heating revealed phase separation in the amorphous state prior to the nucleation of Mg_2Ni nanoparticles. The improved H-storage behavior of the $Mg_{86}N_4Y_{10}$ glass is related to the cracking and pulverization of the alloy pieces when a MgH_2 matrix with finely dispersed $MgNiH_4$ and YH_3 particles develops during hydrogen uptake [22]. The hydrogen storage performance of Mg-Ni-Y alloys can be improved by altering the addition of Ni and Y in order to nucleate a ternary eutectic 14H-LPSO phase; however, this long-period stacking ordered lamellar phase containing Ni and Y atoms does not form after dehydrogenation [23]. High-pressure hydrogen sorption experiments revealed that the as-cast fully amorphous $Mg_{54}Cu_{28}Ag_7Y_{11}$ bulk metallic glass exhibits the largest enthalpy of hydrogen desorption compared to its partially and fully crystallized counterparts; therefore, it was assumed that the disordered local atomic structure of the glass is responsible for the hydrogen release [24]. It was found that the hydrogen storage capacity of fully amorphous melt-spun $Mg_{85}Ni_{15-x}M_x$ (M = Y or La) alloys and their partial devitrified state can exceed 5 wt.% at 300 °C [25]. The hydrogen absorption and desorption kinetics of an amorphous Mg-Y-Ni ternary alloy can be improved when a long-period stacking ordered phase nucleates [26].

Hydrogen absorption of a melt-spun Mg-Ni-Mm alloy promotes the nucleation of a metastable cubic Mg_2NiH_4 phase and the vanishing of its typical monolithic counterpart. With increasing spinning velocity, this tendency becomes more pronounced [27]. The precipitation of the $Mg_{12}Mm$ intermetallic phase in the melt-spun Mg-Ni-Mm (Mm = Ce, La) system preferentially occurs at the Mg grain boundaries, which provide pathways for accelerated hydrogen diffusion [28]. The applied quenching rate has a significant influence on the sorption properties of these alloys [28,29]. When La substitutes Ni in the $Mg_{98}Ni_{2-x}Ce_x$ system, the formation of a refined eutectic structure facilitates hydrogenation. High-density LaH_3 nanoparticles nucleated in situ are responsible for the improved desorption processes [30].

An Mg-Mg_2Ni-LaH_x nanocomposite material formed from the hydrogen-induced decomposition of $Mg_{98}Ni_{1.67}La_{0.33}$ exhibits a H-storage capacity as high as 7.2 wt.% H_2. The significantly reduced absorption activation energy is attributed to the LaH_x and Mg_2Ni nanoparticles embedded in the eutectic alloy [31]. In situ X-ray synchrotron radiation of the Mg-Ni-La system during hydrogenation revealed the formation of a previously non-reported $La_2Mg_{17}H_{\sim 1.0}$ solid solution [32]. The electrochemical performance of a $LaMgNi_4$ electrode reveals acceptable cycling stability, decreasing to 47% of its initial capacity after

250 cycles [33]. It was confirmed that considerable H-induced amorphization occurs during the first sorption cycle, while the volume fraction of the amorphous component increases with the cycling number. This phenomenon was ascribed to the hydrogen-induced lattice instability. It was reported very recently that phase boundaries in a ternary Mg-Ni-La eutectic alloy can act as preferential nucleation sites for MgH_2 and apparently promote the hydrogenation process [34]. As an alternative method, DC magnetron sputtering was also applied to produce the fully amorphous $Mg_{85}Ni_{14}Ce_1$ alloy. It was demonstrated that as the thickness of the thin films decreases, the hydrogen sorption kinetics is significantly improved [35]. In addition, these samples possess an excellent cycling ability at 120 °C.

Severe plastic deformation by ball milling of $Mg_{90}Ni_7Ce_3$ not only refines the nanostructured powder but also enhances the creation of an amorphous component, which is beneficial for improving the H-storage kinetics at a temperature as low as 100 °C, at which 3.5 wt.% H_2 can be absorbed within 30 min [36]. A fully crystalline $Mg_{90}Ce_3Ni_4Y_3$ alloy synthesized by induction melting and subsequent HEBM exhibits an altered rate-limiting step of hydrogen desorption with respect to the host $Mg_{90}Ce_{10}$ intermetallic compound; i.e., the surface-controlled mode is transformed into nucleation- and growth-controlled. The addition of Ni and Y induces a large number of interface channels and nucleation sites [37]. Silver addition by HEBM to Mg_2Ni results in the formation of a hypereutectic Mg-Ni-Ag alloy with an increased cell parameter with respect to Mg_2Ni, which facilitates the diffusion of hydrogen atoms, reduces the onset of dehydrogenation and decreases its activation energy [38]. Very recently, different nanotube additives added by ball milling were proved to successfully improve the H-storage performance of Mg-based systems. For example, when multiwall carbon nanotubes (CNTs) were milled with a Mg-Ni-La alloy, a significant decrease in the dehydrogenation energy (82 kJ/mol) was observed due to the dispersed distribution of the nanotube sections on the surface of Mg-based particles [39].

The hydrogenation performance of different non-equilibrium alloys can be significantly improved when the material is subjected to a massive severe plastic deformation technique called high-pressure torsion (HPT) [40–46]. Among the different deformation methods, HPT exhibits the largest equivalent strain [47]. A $Mg_{65}Ni_{20}Cu_5Ce_{10}$ metallic glass synthesized by rapid quenching and additional torsional straining by HPT possesses a reduced dehydrogenation temperature and improved H-sorption kinetics that can be attributed to the interfaces between different nanoglass regions developed during the HPT process [48]. HPT on a fully amorphous $Mg_{65}Ni_{20}Cu_5Y_{10}$ glass promotes the nucleation of deformation-induced Mg_2Ni nanocrystals, which lowers the hydrogen absorption temperature and increases the storage capacity [49]. It was observed that these phenomena are more pronounced in the most deformed regions of samples [50].

In the current research, an amorphous $Mg_{65}Ni_{20}Cu_5Y_{10}$ glassy ribbon was produced by melt spinning. Glassy flakes of the as-quenched ribbon were milled together with 5 wt.% multiwall carbon nanotubes and were subsequently exposed to HPT with different numbers of whole turns. We demonstrate the structural and thermal stability of these Mg-based composites against severe shear deformation by HPT and shed light on the effect of CNT addition on their electrochemical H-storage performance. The aim of this series of investigations is to demonstrate whether carbon nanotubes can improve the hydrogen storage performance of Mg-based metallic glass, similar to crystalline alloys.

2. Materials and Methods

2.1. Sample Preparation

An ingot of the master alloy with a nominal composition of $Mg_{65}Ni_{20}Cu_5Y_{10}$ was synthesized by induction melting under a protective argon atmosphere. The purity of the constituents was 99.9%. From the ingot, a fully amorphous ribbon (thickness: ~50 μm) was prepared by rapid quenching of the molten alloy using copper single roller planar flow casting in an inert atmosphere. The tangential velocity of the casting wheel was 40 m/s. Subsequently, the as-quenched ribbon was reduced to small pieces (flakes) in a special attritor device, and then these flakes were milled together with 5 wt.% multiwall carbon nanotubes (Sigma-Aldrich, St. Louis, MO, USA; purity 98%; outer diameter: 6–13 nm; length: 2.5–20 μm) in a stainless-steel vial in an SPEX 8000M mixer mill using ten stainless steel balls (1/4 in.) at 1425 rpm, with a ball-to-powder weight ratio of 10:1 under a protective Ar atmosphere. Based on preliminary experiments [45], the total milling time was selected as 15 min in order to ensure a homogeneous mixture while avoiding unnecessary damage to CNT sections. Thereafter, the $Mg_{65}Ni_{20}Cu_5Y_{10}$ + CNT mixture was pre-compacted into cylindrical disks with a radius of R = 4 mm.

High-pressure torsion of the pre-compacted disks was performed under a 4 GPa applied pressure at room temperature while simultaneously imposing shear strain through N = 1, N = 2 and N = 5 whole revolutions with a torsional speed of 1 rot/min. These revolution numbers are typical in the literature. Hereafter, these samples are denoted as MgNiCuY_CNT_1, MgNiCuY_CNT_2 and MgNiCuY_CNT_5. As a comparison, a disk without torsion was also tested (N = 0), which is denoted as MgNiCuY_CNT_0. As a reference, a CNT-free disk tested with N = 5 whole turns was also prepared (MgNiCuY_5). In the applied setup, stainless steel anvils obey a constrained geometry [51]. Further details of HPT processing are given elsewhere [51]. The final thickness of the strained disks is about L = 0.8 mm. The accumulated shear strain for torsion deformation at a radius r at time t can be represented by

$$\varepsilon(r,t) = \frac{\omega \cdot t \cdot r}{L} = 2\pi \frac{N \cdot r}{L} \quad (1)$$

where ω is the angular velocity [51]. At the perimeter of our disk samples, the shear strain can reach extraordinary values, such as $\varepsilon(R) \approx 1200$.

2.2. Thermal Characterization

A Perkin Elmer power-compensated differential scanning calorimeter (DSC) was applied to explore the thermal stability and crystallization behavior of the rapidly quenched $Mg_{65}Ni_{20}Cu_5Y_{10}$ ribbon and the deformed HPT disk during continuous heating carried out at scan rates of 5, 10, 20, 40 and 80 $Kmin^{-1}$. The corresponding ΔH crystallization enthalpy values were determined as the area of exothermic peaks. All measurements were carried out under a protective Ar atmosphere. The temperature and the enthalpy were calibrated by using pure In and Al. The activation energy (E_a) of the crystallization processes was determined by the Kissinger analysis [52]. As is known, the dependence of the individual transformation peak temperature (T_i) on the heating rate can be given as

$$\frac{\beta}{T_i^2} = \frac{Z_i R}{E_{a,i}} \exp\left(\frac{-E_{a,i}}{RT_i}\right) \quad (2)$$

where Z and R are the frequency factor and the gas constant, respectively [50]. Plotting $\ln(\beta/T_i^2)$ vs. T_i^{-1} enables the determination of E_a for each thermal event from the slope of the fitted straight line.

2.3. Structural Characterization

The structures of the as-quenched $Mg_{65}Ni_{20}Cu_5Y_{10}$ glass and the torqued disks were examined by X-ray powder diffraction. The measurements were carried out on a Rigaku SmartLab diffractometer using Cu-Kα radiation in θ–2θ geometry. The data were collected from 20° to 100° with a step size of 0.01°.

2.4. Transmission Electron Microscopy

The local structure of the most deformed CNT-containing MgNiCuY_CNT_5 disk was analyzed by high-resolution transmission electron microscopy (HR-TEM). For this purpose, a THEMIS 200 electron microscope was used at an accelerating voltage of 200 kV. Sample preparation was carried out by cutting out a thin lamella from the HPT disk (close to the perimeter) via focused ion beam (FIB) in an FEI QUANTA 3D dual-beam scanning electron microscope. In order to analyze HR-TEM images and to identify the spatial distribution of crystallites, the fast Fourier transform of the images and the corresponding inverse fast Fourier transform (using Fourier filtering) were produced, respectively. For image processing, the Digital Micrograph (Gatan) software (DigitalMicrograph 3.5, Gatan, Inc., Pleasanton, CA, USA) was used. The elemental distribution of the specimen was investigated by energy-dispersive spectroscopy (EDS) built into the TEM device. High-angle annular dark field (HAADF) scanning transmission (STEM) imaging and line EDS scans were also carried out to visualize local elemental concentration variations.

2.5. Electrochemical Hydriding

Electrochemical hydriding/dehydriding experiments were carried out in a three-electrode cell with Hg/HgO as a reference electrode and a counter electrode prepared from Ni mesh. The metal hydride electrode was prepared by mixing the alloy powder (70 mg) with 100 mg of Teflonized carbon black (VULCAN 72 10%PTFE). Pellets with a diameter of 10 mm and thickness of about 1.5 mm were obtained by pressing the as-prepared mixture with a pressure of 150 atm. The electrolyte was a 6 M KOH water solution. Electrochemical charging and discharging were conducted using a galvanostat/potentiostat at a constant current density of 50 mA/g and 20 mA/g, respectively. Room temperature and a cut-off voltage of 500 mV were applied. Two experiments were performed for each sample.

3. Results and Discussion

3.1. Characterization of the As-Spun Ribbon

The XRD pattern of the as-quenched $Mg_{65}Ni_{20}Cu_5Y_{10}$ ribbon is characterized by a significant halo (2 θ~38 deg), which confirms that the alloy is X-ray amorphous (Figure 1). The corresponding linear heating DSC thermogram exhibits typical features of a metallic glass, including the glass transition (T_g = 439K), followed by a three-stage crystallization sequence characterized by T_{x1} = 471 K, T_{x2} = 579 K and T_{x3} = 648 K exothermic transformations (see Figure 2). The width of the supercooled liquid region obtained as $\Delta T_x = T_{x1,onset} - T_g$ corresponds to a remarkably high GFA (ΔT_x = 32 K), in accordance with other Mg-based glasses [24]. The high value of ΔT_x suggests that the undercooled liquid may have a strong resistance to crystallization either by thermal activation or by SPD. The apparent activation energy values of the T_{x1}, T_{x2} and T_{x3} crystallization transformations were determined from the slope of the Kissinger plot (see the inset of Figure 2), and the obtained values ($E_{a,Tx1}$ = 210 kJ/mol, $E_{a,Tx1}$ = 188 kJ/mol and $E_{a,Tx1}$ = 312 kJ/mol) also indicate high thermal stability, with these values being slightly higher than those obtained for $Mg_{54}Cu_{28}Ag_7Y_{11}$ [24]. The total enthalpy release (ΔH) corresponding to the multi-step crystallization process is ΔH = 105 J/g.

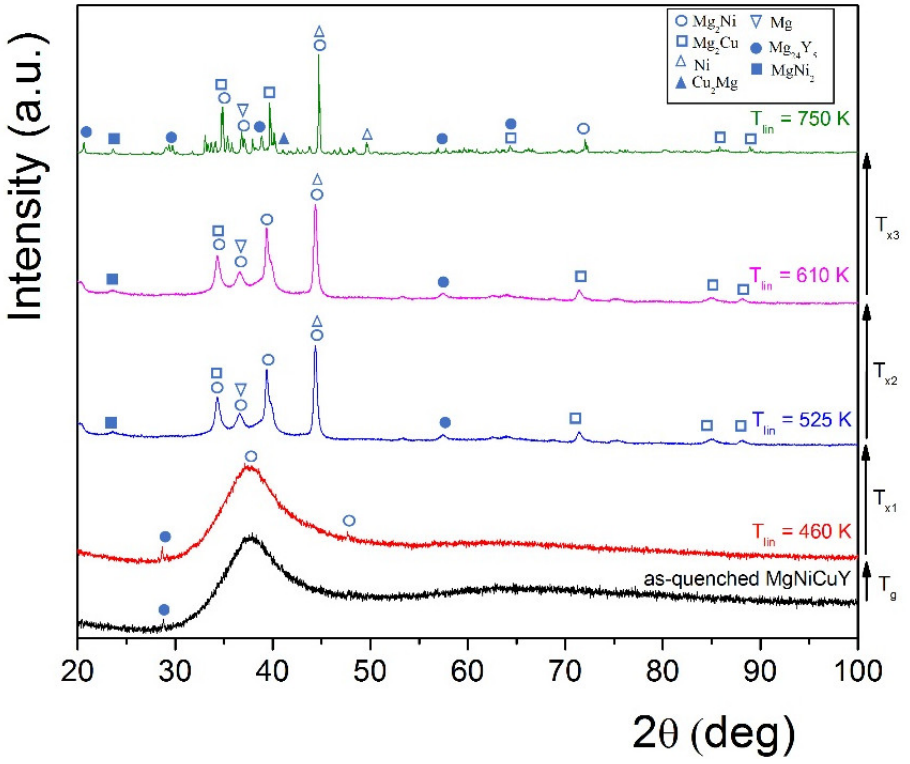

Figure 1. X-ray diffraction patterns for as-quenched $Mg_{65}Ni_{20}Cu_5Y_{10}$ metallic glass and after continuous heating to the indicated temperatures.

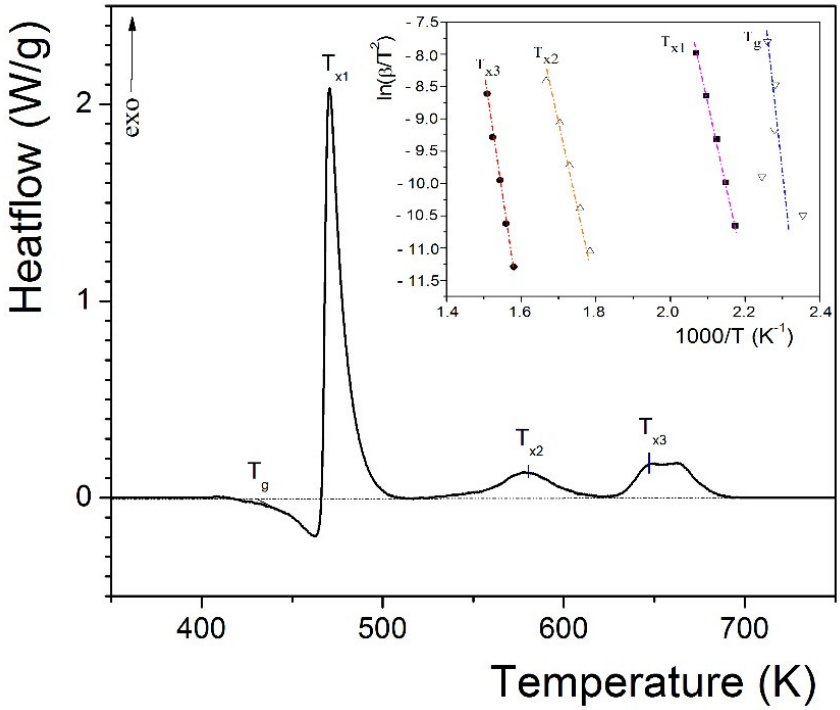

Figure 2. Continuous-heating DSC curve of the as-quenched $Mg_{65}Ni_{20}Cu_5Y_{10}$ metallic glass obtained at 20 $Kmin^{-1}$. The inset shows Kissinger plots.

The evolution of the structure during the crystallization process can be inferred from the corresponding XRD patterns (Figure 1). As one can notice, linear heating above the glass transition preserves the amorphous nature of the alloy; however, very faint peaks corresponding to Mg_2Ni (JCPDS 35-1225; a = 5.21 Å; c = 13.323 Å) appear on the halo.

The complete disappearance of the amorphous background takes place after the first crystallization event (T_{lin}=525 K), while several crystalline phases develop, such as: Mg_2Cu (JCPDS 02-1315; a = 5.273 Å; b = 9.05 Å; c = 18.21 Å), Ni (JCPDS 04-0850: a = 3.5238 Å), Mg (JCPDS 35-0821; a = 3.2093 Å; c = 5.211 Å), $MgNi_2$ (JCPDS 03-1027; a = 4.815 Å; c = 15.80 Å) and $Mg_{24}Y_5$. As can be seen, the XRD pattern of the T_{lin} = 610 K state is almost identical to that of T_{lin} = 525 K, indicating that no crystalline phase nucleation occurs during the T_{x2} transformation. The pattern taken at T_{lin} = 750 K reveals the formation of additional phases, including Cu_2Mg (JCPDS 03-0987; a = 6.99 Å). However, several low-intensity Bragg peaks cannot be indexed.

3.2. Characterization of HPT-Treated and CNT-Catalyzed $Mg_{65}Ni_{20}Cu_5Y_{10}$

Figure 3 presents an optical micrograph taken on the cross-section of the MgNiCuY_CNT_5 disk. As can be seen, the HPT disk exhibits a constant thickness throughout its whole diameter. However, a small material outflow is recognized at the perimeter. The amorphous alloy shows a featureless, homogeneous microstructure without any detectable cracks, indicating almost full compaction of the glassy flakes into the bulk disk.

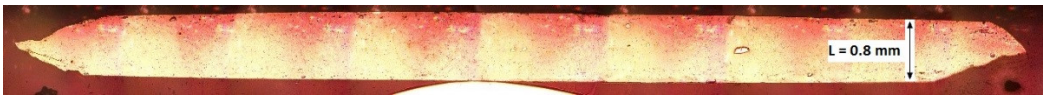

Figure 3. Optical micrograph taken on the cross-section of the HPT disk obtained after N = 5 rotations.

The XRD patterns recorded on the surface of HPT disks exposed to uniaxial compression (MgNiCuY_CNT_0) and varying rotational strains (MgNiCuY_CNT_1, MgNiCuY_CNT_2, MgNiCuY_CNT_5 and MgNiCuY_5) are reported in Figure 4. Similar to the as-quenched glass, all deformed specimens possess the same amorphous halo centered at 2θ ≈ 37 deg, while only very faint Bragg peaks of the Mg_2Ni line compound superimpose on the amorphous background. The intensity of these peaks slightly increases with increased torsional straining; however, the amorphous component becomes dominant throughout the whole deformation process. No Bragg peaks corresponding to the CNT additive are recognized in the pattern. In addition, the MgNiCuY_5 disk probably exhibits other crystalline phases, such as Mg_2Cu and $MgCu_2$, as well. As a consequence, the CNT-containing $Mg_{65}Ni_{20}Cu_5Y_{10}$ glass is extremely stable against deformation-induced devitrification and subsequent crystallization.

In addition to its extreme microstructural stability, the $Mg_{65}Ni_{20}Cu_5Y_{10}$ glassy alloy also exhibits remarkable thermal stability against severe shear deformation during HPT, as confirmed by Figure 5. It is evident from the figure that the continuous-heating DSC thermograms of the HPT-treated disks are very similar to those of the as-quenched ribbon: i.e., each measurement presents T_g and subsequent T_{x1}, T_{x2} and T_{x3} transformations. At the same time, the total heat release (ΔH_{HPT}) for the HPT disk monotonously decreases with the torsion number, and all values are smaller than ΔH obtained for the rapidly quenched glass (see Table 1). If we suppose that the total heat release ΔH corresponds only to the complete amorphous → crystalline transformation [53], the $\Delta H_{HPT}/\Delta H$ ratio should provide the residual amorphous content of the HPT-deformed disks. Accordingly, the crystalline fraction of the partially crystallized state can be written as

$$\eta = 1 - \frac{\Delta H_{HPT}}{\Delta H} \quad (3)$$

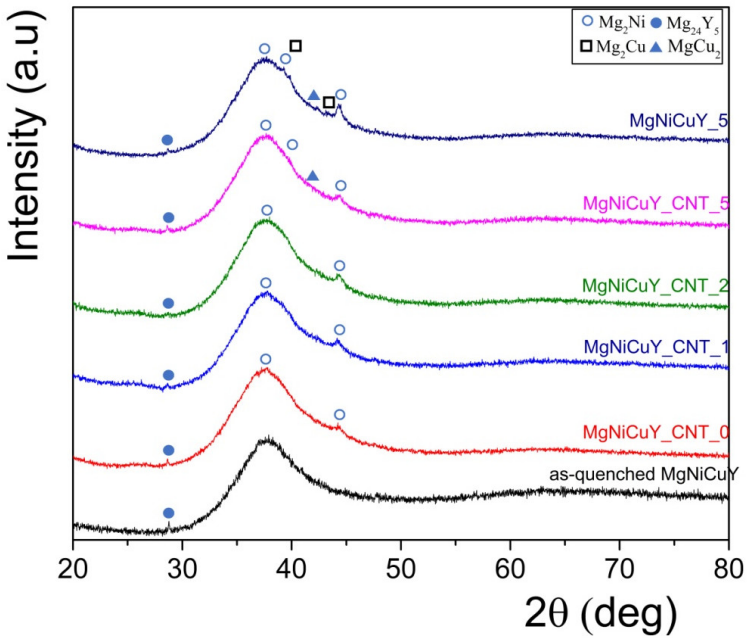

Figure 4. XRD patterns recorded on $Mg_{65}Ni_{20}Cu_5Y_{10}$ HPT disks and the as-quenched ribbon.

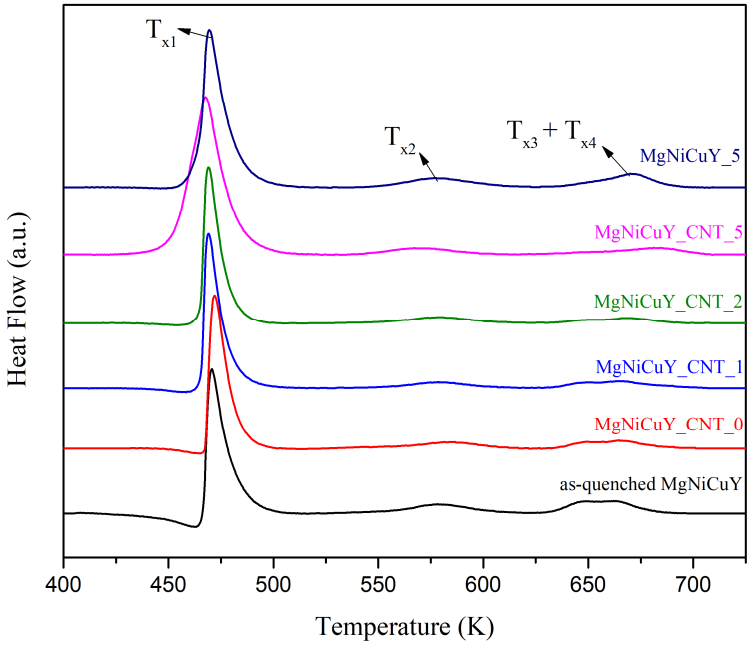

Figure 5. Continuous-heating DSC curves corresponding to the as-quenched $Mg_{65}Ni_{20}Cu_5Y_{10}$ alloy and CNT-containing HPT disks.

The corresponding η values are also listed in Table 1 and presented in Figure 6 as a function of the torsion number. At first glance, it is evident that severe plastic deformation promotes the intensive nucleation of nanocrystals from the amorphous matrix. As one can recognize, the as-pressed MgNiCuY_CNT_0 disk exhibits only 2% extra crystallinity with respect to the as-quenched state, but η increases significantly with the applied torsion number, reaching a maximum value of η = 0.29 for the MgNiCuY_CNT_5 specimen. At the same time, similar deformation conditions yield slightly smaller crystallinity (η = 0.25) for the CNT-free MgNiCuY_5 alloy. Nonetheless, the massive residual amorphous component undoubtedly confirms the high stability of the $Mg_{65}Ni_{20}Cu_5Y_{10}$ alloy.

Table 1. Total exothermic heat release (ΔH_{HPT}) obtained for the HPT disks and the calculated crystalline fraction (η) values.

Sample	ΔH_{HPT} (J/g)	(η)
MgNiCuY_5	79	0.25
MgNiCuY_CNT_5	74	0.29
MgNiCuY_CNT_2	83	0.2
MgNiCuY_CNT_1	86	0.18
MgNiCuY_CNT_0	103	0.02
As Quenched MgNiCuY	105	

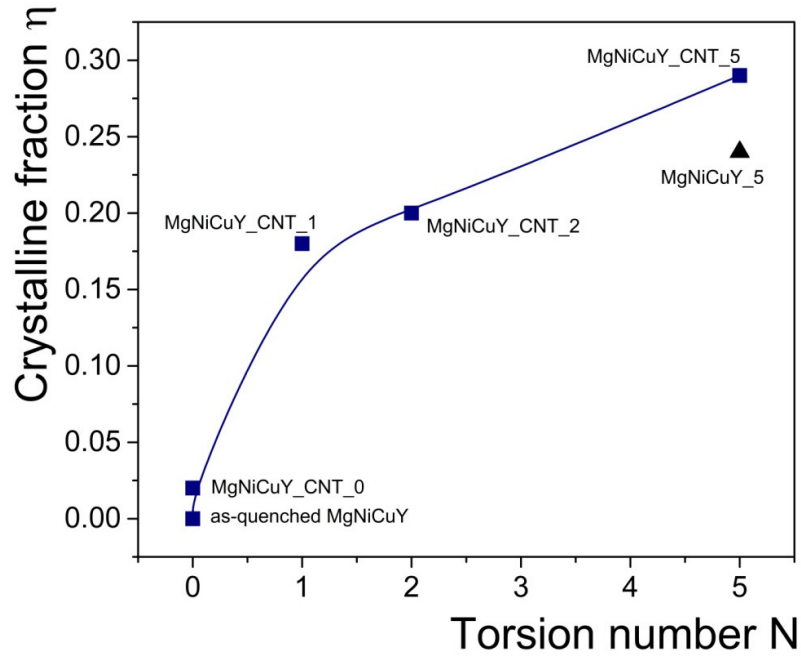

Figure 6. Crystalline fraction obtained for the different HPT disks as a function of the torsion number. The continuous line is a guideline for the eye.

In order to resolve the observed discrepancy between the almost fully amorphous XRD patterns presented in Figure 4 and the reduced amorphous content of the sheared disks, a comprehensive HR-TEM analysis was conducted on the most deformed MgNiCuY_CNT_5 sample.

3.3. TEM Study on the MgNiCuY_CNT_5 HPT Disk

Figure 7a presents a typical HR-TEM micrograph of the MgNiCuY_CNT_5 composite after torsion for $N = 5$ revolutions. It is seen that the material is dominated by an amorphous metal matrix. Lattice fringes of tube-shaped and onion-like carbon structures can also be visualized in the image, which indicates that CNT sections are embedded in this amorphous matrix during SPD processes by HPT. The morphology of the nanotubes suggests severe deformation, since they possess plenty of defects and uneven edges. In the fast Fourier transform of Figure 7a (see the inset), an amorphous halo can be observed, which confirms the disordered structure of the main component of the MgNiCuY_CNT_5 material. Alongside the halo, crystalline Fourier maxima corresponding to the Mg_2Ni phase are also present, in accordance with the XRD study (see Figure 4). The diffraction rings of 2 Å and 1.43 Å can be indexed as (203) and (215), respectively. By using these two Mg_2Ni rings, an inverse Fourier transform image was constructed that displays the spatial distribution of these Mg_2Ni crystals (Figure 7b). Accordingly, crystallites with the size of a few nanometers can be observed in the vicinity of the carbon nanotubes.

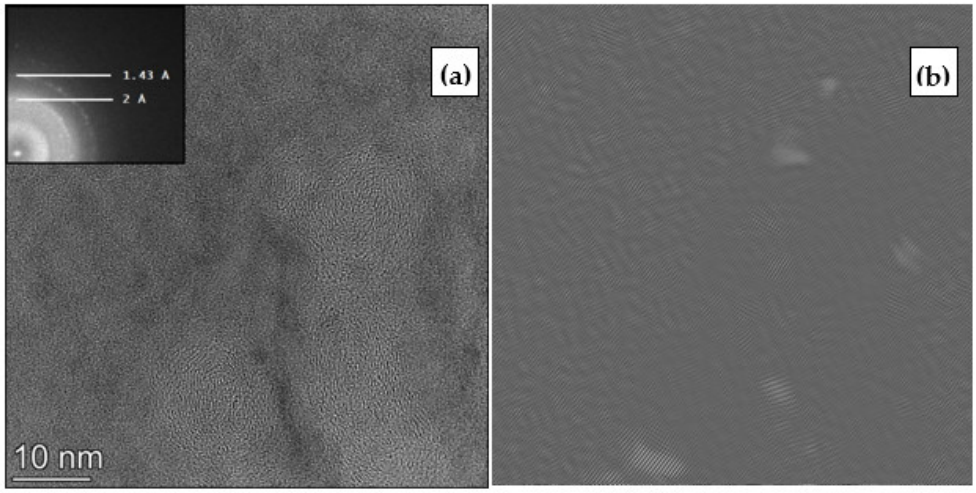

Figure 7. (**a**) HR-TEM micrograph depicting carbon nanotubes embedded in the amorphous matrix of the MgNiCuY_CNT_5 disk. The inset shows the corresponding fast Fourier transform indicating rings of Mg_2Ni Fourier maxima. (**b**) Inverse fast Fourier transform constructed using the 1.43 Å and 2 Å rings of the FFT image.

The HR-TEM image in Figure 8 shows further evidence of deformation-induced nanocrystallization: i.e., parallel atomic rows within a diameter of ~30 nm are clearly seen within a larger crystal. The lattice distance (see inset) matches reasonably well with the d-value of Mg_2Ni.

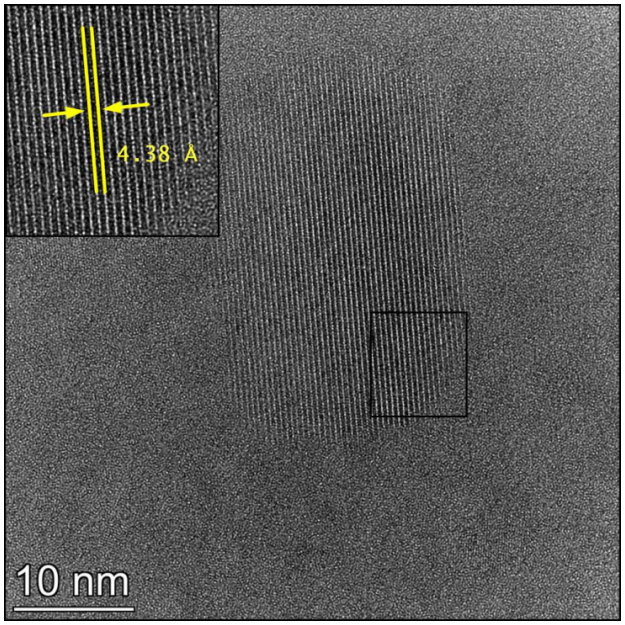

Figure 8. HR-TEM micrograph of a Mg_2Ni crystal embedded in the amorphous matrix of the MgNiCuY_CNT_5 composite. The inset shows a magnified view of the lattice fringe.

A supplementary EDS analysis was also carried out on the MgNiCuY_CNT_5 disk to check for elemental inhomogeneities, which would occur as a result of the precipitation of crystalline phases. The HAADF STEM image in Figure 9a depicts the location of the measurement, which was performed along the line marked by a green arrow. The contrast differences observed in the image already indicate local inhomogeneities. The variation in the measured atomic fractions of the constituting elements along the selected line can be observed in Figure 9b. It is seen that the atomic fractions of Mg and Ni vary significantly

along the line, and their respective values are lower and higher than their nominal compositions (65 at.% and 20 at.%, respectively). It is noted that the systematically lower concentration of Mg (55 at.%) in positions ranging from 60 to 170 nm might be explained by its unavoidable evaporation during the synthesis of the as-quenched glass. There is also some fluctuation in the atomic fraction of Y, but the average value is close to the nominal one (10 at.%). On the other hand, the atomic fraction of Cu is fairly constant along the marked region; nevertheless, its content is significantly higher than in the as-quenched glass (5 at.%). The increased amount of Cu can be explained by contamination (back sputtering) from the TEM lamella sample holder, which occurs during the thinning process. Changes in the local concentrations of Mg and Ni can be better understood by examining the ratio of their atomic fractions (see Figure 9c). It is clearly seen that the measured area is enriched in Ni relative to Mg as compared to their nominal ratio (marked by the dashed line). The remarkably higher Ni concentration on the left-hand side of the selected area coincides with the brighter area in Figure 9a, which corresponds to a higher average atomic number. These observations also support the formation of deformation-induced Mg_2Ni nanocrystals embedded in the residual amorphous matrix.

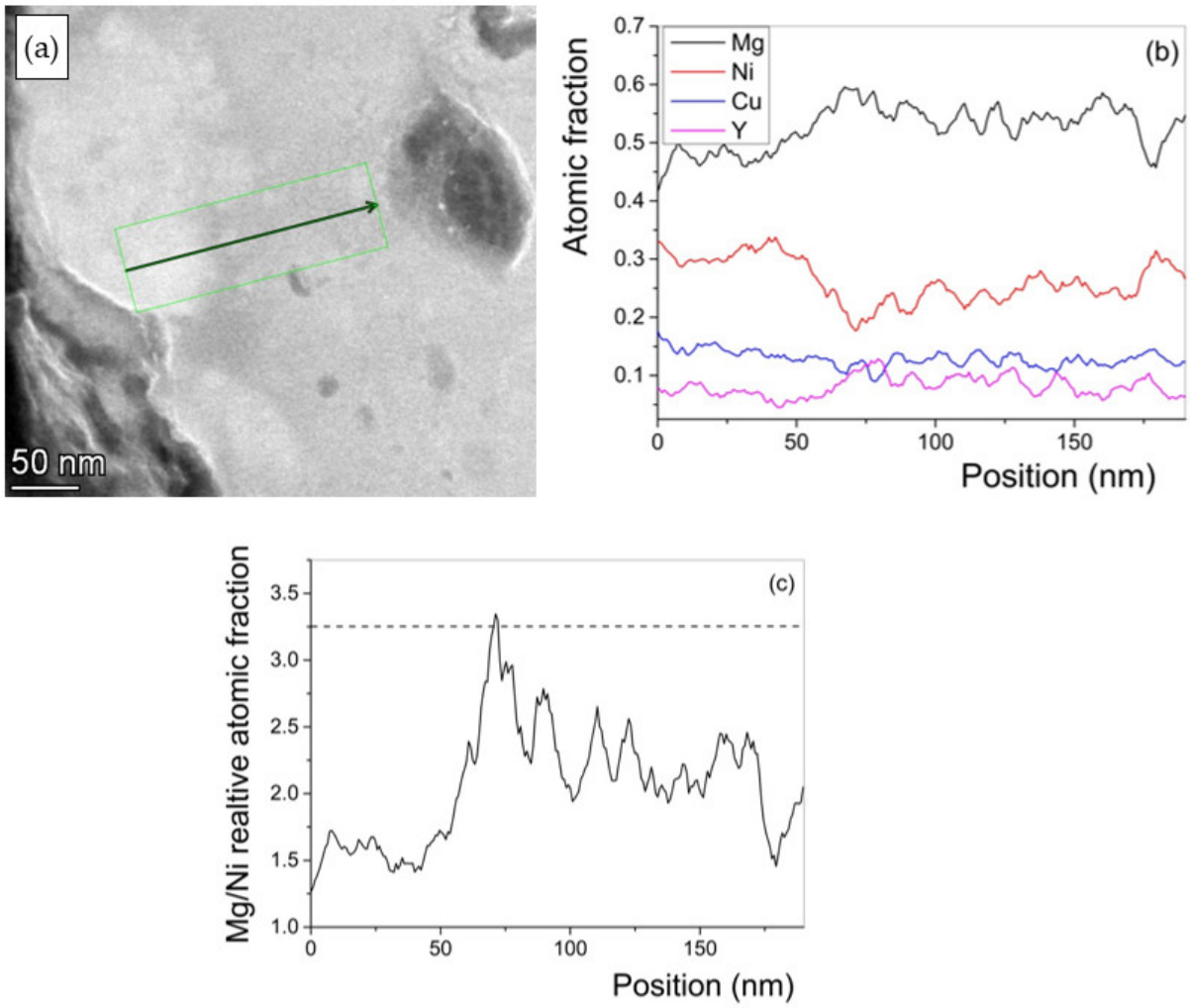

Figure 9. (**a**) HAADF image of the MgNiCuY_CNT_5 disk. The arrow indicates an EDS line measurement. (**b**) Atomic fractions of the constituting elements along the line marked in (**a**). (**c**) Relative atomic fractions of Mg and Ni along the line marked in (**a**); the dashed line indicates the nominal composition.

3.4. Electrochemical Experiments

In order to reveal the hydrogen storage performance of severely deformed amorphous $Mg_{65}Ni_{20}Cu_5Y_{10}$ alloy, electrochemical charge/discharge experiments were carried out at room temperature on the HPT disks. Figure 10 illustrates that all samples containing CNTs exhibit activation after a couple of full charge/discharge cycles, reaching steady-state values of 24–25 mAh/g. These values are slightly lower than those recently obtained for an as-cast Mg-Ni-Cu-La alloy [54]. At the same time, the CNT-free MgNiCuY_5 alloy has a relatively low capacity (<10 mAh/g) over several cycling numbers. Since the capacity of the samples without CNT is substantially lower than that of the samples with CNT, it indicates that CNT plays a key role in the discharge process of Mg-based glasses subjected to severe plastic deformation. As can be seen, MgNiCuY_CNT_0, MgNiCuY_CNT_1 and MgNiCuY_CNT_2 disks reveal a rather similar charge/discharge behavior upon cycling, which might correspond to the similar microstructure obtained in the XRD studies. Interestingly, the most deformed HPT disk (MgNiCuY_CNT_5) shows a slightly lower capacity up to eight cycles, which is followed by a clear breakdown. In our opinion, this phenomenon might be related to the increased density of more damaged CNTs (see Figure 7), which suggests that the best hydrogen absorption performance is associated with the optimal morphology and length of the nanotubes, as was also confirmed for other Mg-based hydrogen absorbing systems [45].

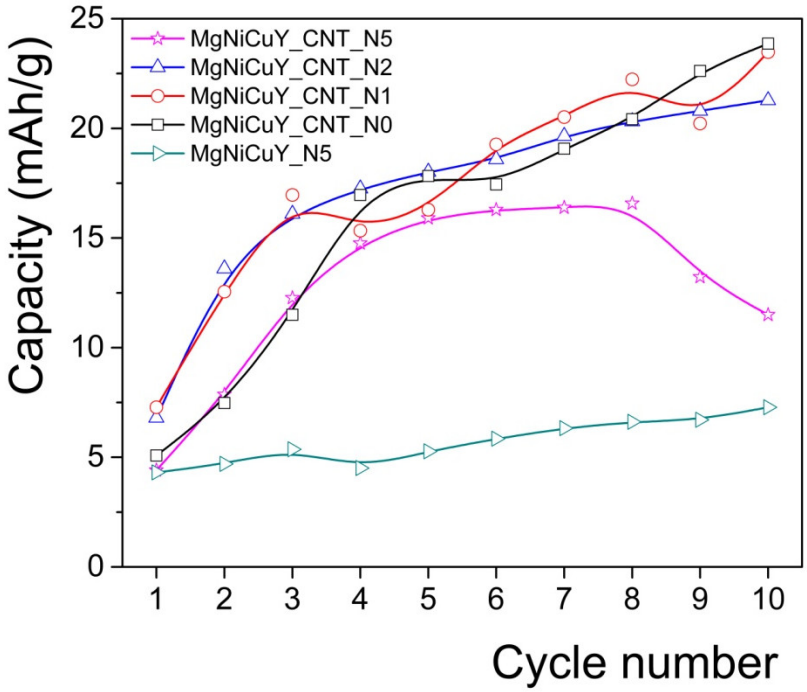

Figure 10. Electrochemical hydriding of MgNiCuY HPT disks.

4. Conclusions

An amorphous $Mg_{65}Ni_{20}Cu_5Y_{10}$ metallic glass with light weight was produced by melt spinning. Amorphous glassy flakes of the as-quenched ribbon were milled together with 5 wt.% multiwall carbon nanotubes and were subsequently exposed to high-pressure torsion with different numbers of whole turns. Complimentary XRD and DSC experiments confirmed the exceptional structural and thermal stability of the glass against the severe plastic deformation generated during HPT. Nevertheless, combined HR-TEM experiments and fast Fourier transform analysis carried out on the most deformed MgNiCuY_CNT_5 disk revealed the formation of deformation-induced Mg_2Ni nanocrystals a few nanometers in size embedded in the amorphous matrix. At the same time, lattice

fringes of tube-shaped and onion-like carbon structures confirmed the structural and morphological stability of the CNT sections. The variation in the atomic fractions of the constituting elements determined by HAADF STEM indicated that some regions are enriched in Ni, in accordance with the formation of Mg_2Ni nanocrystals. The electrochemical hydrogen absorption capacity of the HPT-deformed disk containing no nanotubes (MgNiCuY_5) was substantially lower than that of the samples with the CNT additive for several cycles, which confirms that nanotubes play a crucial role in the absorption of hydrogen by Mg-based glasses subjected to severe plastic deformation. It was also established that the most deformed MgNiCuY_CNT_5 disk exhibited a clear breakdown in the electrochemical capacity after eight cycles, which suggests that there exist an optimal morphology and length of the nanotubes.

Author Contributions: Calorimetry measurements, XRD measurements, HPT processing, and writing and editing, Á.R.; pre-compaction of powders, TEM sample preparation and writing, M.G.; ball milling and evaluation of XRD data, M.A.; TEM experiments, V.K.K.; HPT processing, E.S.; preparation of the master alloy, L.K.V.; electrochemical measurements, S.T. and T.S.; melt spinning, M.B. All authors have read and agreed to the published version of the manuscript.

Funding: The electron microscopy facility at the Centre for Energy Research, Budapest, was funded by the European Structural and Investment Funds, grant no. VEKOP-2.3.3–15–2016–0 0 0 02. M.A. is indebted to the Tempus organization for providing a Stipendium Hungaricum scholarship.

Conflicts of Interest: The authors declare no conflict of interest. The funders had no role in the design of the study; in the collection, analyses or interpretation of data; in the writing of the manuscript; or in the decision to publish the results.

References

1. Ren, J.; Musyoka, N.M.; Langmi, H.W.; Mathe, M.; Liao, S. Current Research Trends and Perspectives on Materials-Based Hydrogen Storage Solutions: A Critical Review. *Int. J. Hydrogen Energy* **2017**, *42*, 289–311. https://doi.org/10.1016/j.ijhydene.2016.11.195.
2. Borgschulte, A. The Hydrogen Grand Challenge. *Front. Energy Res.* **2016**, *4*, 11. https://doi.org/10.3389/fenrg.2016.00011.
3. Schlapbach, L.; Züttel, A. Hydrogen-Storage Materials for Mobile Applications. *Nature* **2001**, *414*, 353–358. https://doi.org/10.1038/35104634.
4. Varin, R.A.; Czujko, T.; Wronski, Z.S. *Nanomaterials for Solid State Hydrogen Storage*; Springer Science: New York, NY, USA, 2009.
5. Aguey-Zinsou, K.-F.; Ares-Fernández, J.-R. Hydrogen in Magnesium: New Perspectives toward Functional Stores. *Energy Environ. Sci.* **2010**, *3*, 526–543. https://doi.org/10.1039/b921645f.
6. Pasquini, L. The Effects of Nanostructure on the Hydrogen Sorption Properties of Magnesium-Based Metallic Compounds: A Review. *Crystals* **2018**, *8*, 106. https://doi.org/10.3390/cryst8020106.
7. Crivello, J.-C.; Dam, B.; Denys, R.V.; Dornheim, M.; Grant, D.M.; Huot, J.; Jensen, T.R.; de Jongh, P.; Latroche, M.; Milanese, C.; et al. Review of Magnesium Hydride-Based Materials: Development and Optimisation. *Appl. Phys. A* **2016**, *122*, 97. https://doi.org/10.1007/s00339-016-9602-0.
8. Révész, Á.; Gajdics, M. Improved H-Storage Performance of Novel Mg-Based Nanocomposites Prepared by High-Energy Ball Milling: A Review. *Energies* **2021**, *14*, 6400. https://doi.org/10.3390/en14196400.
9. Li, J.; Li, B.; Shao, H.; Li, W.; Lin, H. Catalysis and Downsizing in Mg-Based Hydrogen Storage Materials. *Catalysts* **2018**, *8*, 89. https://doi.org/10.3390/catal8020089.
10. Lin, H.-J.; Lu, Y.-S.; Zhang, L.-T.; Liu, H.-Z.; Edalati, K.; Révész, Á. Recent Advances in Metastable Alloys for Hydrogen Storage: A Review. *Rare Met.* **2022**, *41*, 1797–1817. https://doi.org/10.1007/s12598-021-01917-8.
11. Hara, M.; Morozumi, S.; Watanabe, K. Effect of a Magnesium Depletion on the Mg–Ni–Y Alloy Hydrogen Absorption Properties. *J. Alloys Compd.* **2006**, *414*, 207–214. https://doi.org/10.1016/j.jallcom.2005.05.048.
12. Zhang, Y.; Zhao, D.; Li, B.; Ren, H.; Guo, S.; Wang, X. Electrochemical Hydrogen Storage Characteristics of Nanocrystalline $Mg_{20}Ni_{10-x}Co_x$ (X = 0–4) Alloys Prepared by Melt-Spinning. *J. Alloys Compd.* **2010**, *491*, 589–594. https://doi.org/10.1016/j.jallcom.2009.11.013.
13. Si, T.Z.; Liu, Y.F.; Zhang, Q.A. Hydrogen Storage Properties of the Supersaturated $Mg_{12}YNi$ Solid Solution. *J. Alloys Compd.* **2010**, *507*, 489–493. https://doi.org/10.1016/j.jallcom.2010.07.214.
14. Kalinichenka, S.; Röntzsch, L.; Baehtz, C.; Kieback, B. Hydrogen Desorption Kinetics of Melt-Spun and Hydrogenated $Mg_{90}Ni_{10}$ and $Mg_{80}Ni_{10}Y_{10}$ Using in Situ Synchrotron, X-Ray Diffraction and Thermogravimetry. *J. Alloys Compd.* **2010**, *496*, 608–613. https://doi.org/10.1016/j.jallcom.2010.02.128.
15. Spassov, T.; Köster, U. Thermal Stability and Hydriding Properties of Nanocrystalline Melt-Spun $Mg_{63}Ni_{30}Y_7$ Alloy. *J. Alloys Compd.* **1998**, *279*, 279–286. https://doi.org/10.1016/S0925-8388(98)00680-X.

16. Zhang, Q.A.; Jiang, C.J.; Liu, D.D. Comparative Investigations on the Hydrogenation Characteristics and Hydrogen Storage Kinetics of Melt-Spun $Mg_{10}NiR$ (R = La, Nd and Sm) Alloys. *Int. J. Hydrogen Energy* **2012**, *37*, 10709–10714. https://doi.org/10.1016/j.ijhydene.2012.04.038.
17. Huang, L.J.; Wang, H.; Ouyang, L.Z.; Sun, D.L.; Lin, H.J.; Zhu, M. Achieving Fast Hydrogenation by Hydrogen-Induced Phase Separation in Mg-Based Amorphous Alloys. *J. Alloys Compd.* **2021**, *887*, 161476. https://doi.org/10.1016/j.jallcom.2021.161476.
18. Lin, H.-J.; He, M.; Pan, S.-P.; Gu, L.; Li, H.-W.; Wang, H.; Ouyang, L.-Z.; Liu, J.-W.; Ge, T.-P.; Wang, D.-P.; et al. Towards Easily Tunable Hydrogen Storage via a Hydrogen-Induced Glass-to-Glass Transition in Mg-Based Metallic Glasses. *Acta Mater.* **2016**, *120*, 68–74. https://doi.org/10.1016/j.actamat.2016.08.020.
19. Spassov, T.; Köster, U. Hydrogenation of Amorphous and Nanocrystalline Mg-Based Alloys. *J. Alloys Compd.* **1999**, *287*, 243–250. https://doi.org/10.1016/S0925-8388(99)00035-3.
20. Kalinichenka, S.; Röntzsch, L.; Kieback, B. Structural and Hydrogen Storage Properties of Melt-Spun Mg–Ni–Y Alloys. *Int. J. Hydrogen Energy* **2009**, *34*, 7749–7755. https://doi.org/10.1016/j.ijhydene.2009.07.053.
21. Zhou, H.; Tan, J.; Dong, Q.; Ma, L.F.; Ding, D.Y.; Guo, S.F.; Li, Q.; Chen, Y.A.; Pan, F.S. Nonisothermal Crystallization Behavior of Micron-Sized $Mg_{85}Ni_5Y_{10}$ Amorphous Wires. *J. Non-Cryst. Solids* **2022**, *581*, 121412. https://doi.org/10.1016/j.jnoncrysol.2022.121412.
22. Yang, T.; Wang, P.; Xia, C.; Li, Q.; Liang, C.; Zhang, Y. Characterization of Microstructure, Hydrogen Storage Kinetics and Thermodynamics of a Melt-Spun $Mg_{86}Y_{10}Ni_4$ Alloy. *Int. J. Hydrogen Energy* **2019**, *44*, 6728–6737. https://doi.org/10.1016/j.ijhydene.2019.01.148.
23. Pang, X.; Ran, L.; Chen, Y.; Luo, Y.; Pan, F. Enhancing Hydrogen Storage Performance via Optimizing Y and Ni Element in Magnesium Alloy. *J. Magnes. Alloys* **2022**, *10*, 821–835. https://doi.org/10.1016/j.jma.2021.11.026.
24. Révész, Á.; Kis-Tóth, Á.; Varga, L.K.; Lábár, J.L.; Spassov, T. High Glass Forming Ability Correlated with Microstructure and Hydrogen Storage Properties of a Mg–Cu–Ag–Y Glass. *Int. J. Hydrogen Energy* **2014**, *39*, 9230–9240. https://doi.org/10.1016/j.ijhydene.2014.03.214.
25. Lass, E.A. Hydrogen Storage Measurements in Novel Mg-Based Nanostructured Alloys Produced via Rapid Solidification and Devitrification. *Int. J. Hydrogen Energy* **2011**, *36*, 10787–10796. https://doi.org/10.1016/j.ijhydene.2011.05.137.
26. Zhang, Q.A.; Liu, D.D.; Wang, Q.Q.; Fang, F.; Sun, D.L.; Ouyang, L.Z.; Zhu, M. Superior Hydrogen Storage Kinetics of $Mg_{12}YNi$ Alloy with a Long-Period Stacking Ordered Phase. *Scr. Mater.* **2011**, *65*, 233–236. https://doi.org/10.1016/j.scriptamat.2011.04.014.
27. Wu, Y.; Lototskyy, M.V.; Solberg, J.K.; Yartys, V.A. Effect of Microstructure on the Phase Composition and Hydrogen Absorption-Desorption Behaviour of Melt-Spun Mg-20Ni-8Mm Alloys. *Int. J. Hydrogen Energy* **2012**, *37*, 1495–1508. https://doi.org/10.1016/j.ijhydene.2011.09.126.
28. Wu, Y.; Solberg, J.K.; Yartys, V.A. The Effect of Solidification Rate on Microstructural Evolution of a Melt-Spun Mg–20Ni–8Mm Hydrogen Storage Alloy. *J. Alloys Compd.* **2007**, *446–447*, 178–182. https://doi.org/10.1016/j.jallcom.2006.12.002.
29. Zhang, Y.; Li, B.; Ren, H.; Guo, S.; Zhao, D.; Wang, X. Hydrogenation and Dehydrogenation Behaviours of Nanocrystalline $Mg_{20}Ni_{10-x}Cu_x$ (X = 0–4) Alloys Prepared by Melt Spinning. *Int. J. Hydrogen Energy* **2010**, *35*, 2040–2047. https://doi.org/10.1016/j.ijhydene.2009.12.029.
30. Ding, X.; Chen, R.; Chen, X.; Pu, J.; Su, Y.; Guo, J. Study on the Eutectic Formation and Its Correlation with the Hydrogen Storage Properties of $Mg_{98}Ni_{2-x}La_x$ Alloys. *Int. J. Hydrogen Energy* **2021**, *46*, 17814–17826. https://doi.org/10.1016/j.ijhydene.2021.02.183.
31. Ding, X.; Chen, R.; Zhang, J.; Chen, X.; Su, Y.; Guo, J. Achieving Superior Hydrogen Storage Properties via In-Situ Formed Nanostructures: A High-Capacity Mg–Ni Alloy with La Microalloying. *Int. J. Hydrogen Energy* **2022**, *47*, 6755–6766. https://doi.org/10.1016/j.ijhydene.2021.12.010.
32. Denys, R.V.; Poletaev, A.A.; Maehlen, J.P.; Solberg, J.K.; Tarasov, B.P.; Yartys, V.A. Nanostructured Rapidly Solidified $LaMg_{11}Ni$ Alloy. II. In Situ Synchrotron X-Ray Diffraction Studies of Hydrogen Absorption–Desorption Behaviours. *Int. J. Hydrogen Energy* **2012**, *37*, 5710–5722. https://doi.org/10.1016/j.ijhydene.2011.12.133.
33. Li, H.; Wan, C.; Li, X.; Ju, X. Structural, Hydrogen Storage, and Electrochemical Performance of $LaMgNi_4$ Alloy and Theoretical Investigation of Its Hydrides. *Int. J. Hydrogen Energy* **2022**, *47*, 1723–1734. https://doi.org/10.1016/j.ijhydene.2021.10.135.
34. Guo, F.; Zhang, T.; Shi, L.; Chen, Y.; Song, L. Mechanisms of Hydrides' Nucleation and the Effect of Hydrogen Pressure Induced Driving Force on de-/Hydrogenation Kinetics of Mg-Based Nanocrystalline Alloys. *Int. J. Hydrogen Energy* **2022**, *47*, 1063–1075. https://doi.org/10.1016/j.ijhydene.2021.10.104.
35. Han, B.; Yu, S.; Wang, H.; Lu, Y.; Lin, H.-J. Nanosize Effect on the Hydrogen Storage Properties of Mg-Based Amorphous Alloy. *Scr. Mater.* **2022**, *216*, 114736. https://doi.org/10.1016/j.scriptamat.2022.114736.
36. Song, F.; Yao, J.; Yong, H.; Wang, S.; Xu, X.; Chen, Y.; Zhang, L.; Hu, J. Investigation of Ball-Milling Process on Microstructure, Thermodynamics and Kinetics of Ce–Mg–Ni-Based Hydrogen Storage Alloy. *Int. J. Hydrogen Energy* **2022**, *in press*. https://doi.org/10.1016/j.ijhydene.2022.05.057.
37. Kang, H.; Yong, H.; Wang, J.; Xu, S.; Li, L.; Wang, S.; Hu, J.; Zhang, Y. Characterization on the Kinetics and Thermodynamics of Mg-Based Hydrogen Storage Alloy by the Multiple Alloying of Ce, Ni and Y Elements. *Mater. Charact.* **2021**, *182*, 111583. https://doi.org/10.1016/j.matchar.2021.111583.
38. Cao, W.; Ding, X.; Zhang, Y.; Zhang, J.; Chen, R.; Su, Y.; Guo, J.; Fu, H. Enhanced De-/Hydrogenation Kinetics of a Hyper-Eutectic $Mg_{85}Ni_{15-x}Ag_x$ Alloy Facilitated by Ag Dissolving in Mg_2Ni. *J. Alloys Compd.* **2022**, *917*, 165457. https://doi.org/10.1016/j.jallcom.2022.165457.

39. Guo, F.; Zhang, T.; Shi, L.; Chen, Y.; Song, L. Ameliorated Microstructure and Hydrogen Absorption/Desorption Properties of Novel Mg–Ni–La Alloy Doped with MWCNTs and Co Nanoparticles. *Int. J. Hydrogen Energy* **2022**, *47*, 18044–18057. https://doi.org/10.1016/j.ijhydene.2022.03.263.
40. Révész, Á.; Gajdics, M. High-Pressure Torsion of Non-Equilibrium Hydrogen Storage Materials: A Review. *Energies* **2021**, *14*, 819. https://doi.org/10.3390/en14040819.
41. Révész, Á.; Kovács, Z. Severe Plastic Deformation of Amorphous Alloys. *Mater. Trans.* **2019**, *60*, 1283–1293. https://doi.org/10.2320/matertrans.MF201917.
42. Edalati, K.; Bachmaier, A.; Beloshenko, V.A.; Beygelzimer, Y.; Blank, V.D.; Botta, W.J.; Bryła, K.; Čížek, J.; Divinski, S.; Enikeev, N.A.; et al. Nanomaterials by Severe Plastic Deformation: Review of Historical Developments and Recent Advances. *Mater. Res. Lett.* **2022**, *10*, 163–256. https://doi.org/10.1080/21663831.2022.2029779.
43. Strozi, R.B.; Ivanisenko, J.; Koudriachova, N.; Huot, J. Effect of HPT on the First Hydrogenation of $LaNi_5$ Metal Hydride. *Energies* **2021**, *14*, 6710. https://doi.org/10.3390/en14206710.
44. Chu, F.; Wu, K.; Meng, Y.; Edalati, K.; Lin, H.-J. Effect of High-Pressure Torsion on the Hydrogen Evolution Performances of a Melt-Spun Amorphous $Fe_{73.5}Si_{13.5}B_9Cu_1Nb_3$ Alloy. *Int. J. Hydrogen Energy* **2021**, *46*, 25029–25038. https://doi.org/10.1016/j.ijhydene.2021.05.042.
45. Gajdics, M.; Spassov, T.; Kis, V.K.; Schafler, E.; Révész, Á. Microstructural and Morphological Investigations on Mg-Nb_2O_5-CNT Nanocomposites Processed by High-Pressure Torsion for Hydrogen Storage Applications. *Int. J. Hydrogen Energy* **2020**, *45*, 7917–7928. https://doi.org/10.1016/j.ijhydene.2019.06.165.
46. Gajdics, M.; Spassov, T.; Kovács Kis, V.; Béke, F.; Novák, Z.; Schafler, E.; Révész, Á. Microstructural Investigation of Nanocrystalline Hydrogen-Storing Mg-Titanate Nanotube Composites Processed by High-Pressure Torsion. *Energies* **2020**, *13*, 563. https://doi.org/10.3390/en13030563.
47. Valiev, R.Z.; Islamgaliev, R.K.; Alexandrov, I.V. Bulk Nanostructured Materials from Severe Plastic Deformation. *Prog. Mater. Sci.* **2000**, *45*, 103–189. https://doi.org/10.1016/S0079-6425(99)00007-9.
48. Xu, C.; Lin, H.-J.; Edalati, K.; Li, W.; Li, L.; Zhu, Y. Superior Hydrogenation Properties in a $Mg_{65}Ce_{10}Ni_{20}Cu_5$ Nanoglass Processed by Melt-Spinning Followed by High-Pressure Torsion. *Scr. Mater.* **2018**, *152*, 137–140. https://doi.org/10.1016/j.scriptamat.2018.04.036.
49. Révész, Á.; Kis-Tóth, Á.; Szommer, P.; Spassov, T. Hydrogen Storage, Microstructure and Mechanical Properties of Strained $Mg_{65}Ni_{20}Cu_5Y_{10}$ Metallic Glass. *Mater. Sci. Forum* **2013**, *729*, 74–79. https://doi.org/10.4028/www.scientific.net/MSF.729.74.
50. Révész, Á.; Kis-Tóth, Á.; Varga, L.K.; Schafler, E.; Bakonyi, I.; Spassov, T. Hydrogen Storage of Melt-Spun Amorphous $Mg_{65}Ni_{20}Cu_5Y_{10}$ Alloy Deformed by High-Pressure Torsion. *Int. J. Hydrogen Energy* **2012**, *37*, 5769–5776. https://doi.org/10.1016/j.ijhydene.2011.12.160.
51. Zhilyaev, A.; Langdon, T. Using High-Pressure Torsion for Metal Processing: Fundamentals and Applications. *Prog. Mater. Sci.* **2008**, *53*, 893–979. https://doi.org/10.1016/j.pmatsci.2008.03.002.
52. Kissinger, H.E. Reaction Kinetics in Differential Thermal Analysis. *Anal. Chem.* **1957**, *29*, 1702–1706. https://doi.org/10.1021/ac60131a045.
53. Jiang, J.Z.; Kato, H.; Ohsuna, T.; Saida, J.; Inoue, A.; Saksl, K.; Franz, H.; Ståhl, K. Origin of Nondetectable X-Ray Diffraction Peaks in Nanocomposite CuTiZr Alloys. *Appl. Phys. Lett.* **2003**, *83*, 3299–3301. https://doi.org/10.1063/1.1619220.
54. Hou, Z.; Zhang, W.; Wei, X.; Yuan, Z.; Ge, Q. Hydrogen Storage Behavior of Nanocrystalline and Amorphous Mg–Ni–Cu–La Alloys. *RSC Adv.* **2020**, *10*, 33103–33111. https://doi.org/10.1039/D0RA05417H.